Formation and growth characteristics of co-culture tumour spheroids

Ryan J. Murphy[1,*], Gency Gunasingh[2], Nikolas K. Haass[2,†], Matthew J. Simpson[1,†]

[1] *Mathematical Sciences, Queensland University of Technology, Brisbane, Australia*

[2] *Frazer Institute, The University of Queensland, Brisbane, Australia*

Abstract

Co-culture tumour spheroid experiments are routinely performed to investigate cancer progression and test anti-cancer therapies. Therefore, methods to characterise and interpret co-culture spheroid growth are of great interest. However, co-culture spheroid growth is complex. Multiple biological processes occur on overlapping timescales and different cell types within the spheroid may have different characteristics, for example proliferation rate or response to nutrient availability. There is no standard, widely-accepted mathematical model of such complex spatio-temporal growth processes. Typical approaches to analyse these experiments focus on the late-time temporal evolution of spheroid size and overlook early-time spheroid formation, spheroid structure and geometry. Here we make theoretical and practical contributions. We develop a general framework, based on mathematical and statistical modelling, to analyse a series of co-culture experiments. Using a range of different mathematical models we provide new biological insights about spheroid formation, growth, and structure. In addition, we extend a general class of compartment-based monoculture spheroid mathematical models to describe multiple populations and provide mechanistic biological insight. The framework is well-suited to analyse spheroids grown with multiple different cell types and the new class of mathematical models provide opportunities for further mathematical and biological insights.

Key words: mathematical modelling, parameter estimation, profile likelihood analysis, cancer, heterogeneous population growth.

*Corresponding author: r23.murphy@qut.edu.au

†These authors contributed equally.

1 Introduction

Tumour spheroids are a key experimental tool to study cancer progression and to develop cancer therapies [1, 2, 3, 4]. Spheroids also bridge the gap between two-dimensional *in vitro* experiments and three-dimensional *in vivo* experiments. Previously we have developed a framework to characterise the temporal evolution of monoculture spheroid size and structure [5, 6, 7]. Here, we focus on more complicated co-culture tumour spheroid experiments. These experiments are performed with two cell types, melanoma cells and fibroblasts. Each cell type may exhibit different characteristics, for example different proliferation rates or different responses to nutrient availability. Further, within each spheroid multiple biological processes occur on overlapping timescales. Therefore, characterising and interpreting co-culture spheroid growth is challenging. To address this challenge, we develop a general framework based on mathematical and statistical modelling. Throughout we provide novel practical and theoretical contributions. This includes characterising and interpreting co-culture spheroid formation and growth and extending a general class of monoculture compartment-based mathematical models to multiple populations to provide mechanistic biological insight.

Co-culture spheroid experiments are routinely performed to capture some of the complexity of *in situ* tumours, in particular the growth and interactions of multiple cell types [8, 9, 10, 11]. Here, we grow cancer cell line spheroids and incorporate a second cell type, fibroblasts, to enhance spheroid formation and geometry and to explore the impact of the second cell type on growth [10, 11]. To perform our experiments, we place a mixture of melanoma cells and fibroblasts into a well of a cell culture plate. The cells then adhere and migrate to form a three-dimensional compact solid mass, i.e. a spheroid, whose overall size grows in a sigmoidal manner over time (Fig 1A,B) [12, 13]. In the first set of experiments we focus on early time spheroid formation, geometry, and growth. In a second set of experiments we focus on later time temporal evolution of spheroid size and structure. Experimental measurements are obtained by analysing top-down brightfield images, confocal microscopy images of each spheroid's equatorial plane, and three dimensional spheroid renderings from confocal microscopy z-stacks.

To explore early time spheroid formation and subsequent sigmoidal growth, we consider a biphasic mathematical model (Fig 1C) [14]. In each of the two phases, namely formation and growth, the size of the spheroid is described by an ordinary differential equation. This allows us to estimate spheroid formation time and extends traditional analysis that overlook formation [15, 16, 17]. Early time growth dynamics are reasonably described with a linear model (Fig 1D). We connect each mathematical model to experimental data using statistical modelling. Specifically, we use profile likelihood analysis for parameter estimation, to form approximate confidence intervals, and to assess if parameters are *practically identifiable* [6, 14, 17, 18, 19, 20]. A parameter is practically identifiable if it can be uniquely identified given a finite set of noisy experimental data. This is in contrast to *structural identifiability* studies that assess whether parameters can be uniquely identified given a set of continuous noise-free observations [20].

In a second set of experiments we focus on the temporal evolution of spheroid structure. In monoculture spheroid experiments, growth after formation can be characterised by two phases. First, at early

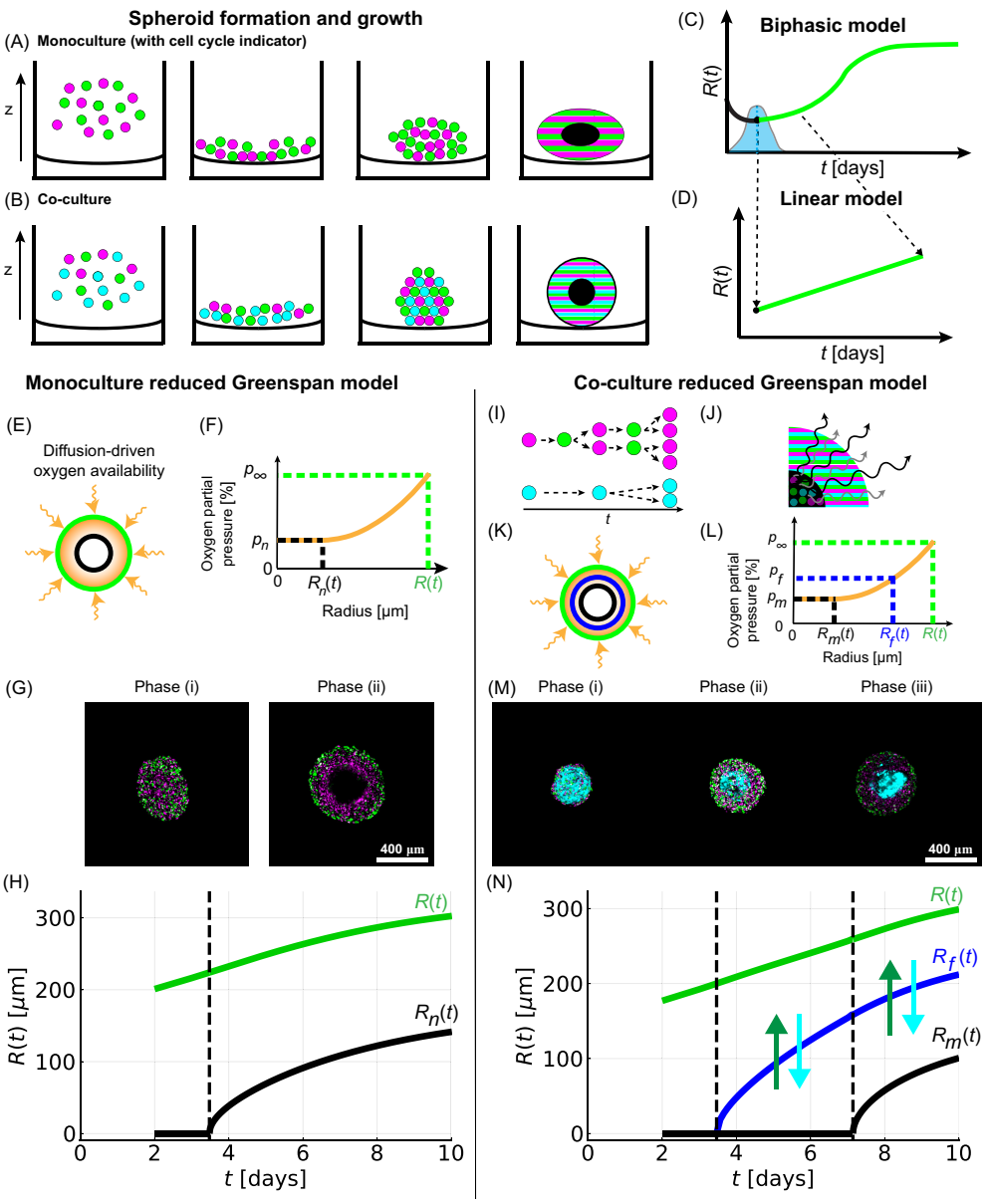

Figure 1: Characterising co-culture tumour spheroid growth using mechanistic mathematical modelling. (A-B) Spheroid formation and growth schematics. Cells placed into a well adhere and migrate to form a spheroid which then grows. Dots represent cells, striped shading represents regions of multiple cell types, and black circles represent necrotic core. (A) Monoculture with cell cycle indicator (FUCCI). Throughout, colours represent FUCCI signals observed in experimental images, e.g. (G): cells in gap 1 (G1) phase fluoresce red, shown in magenta for clarity; and cells in synthesis, gap 2, and mitotic (S/G2/M) phases fluoresce green (B) Co-culture with two cell types: one cell type (melanoma) with cell cycle indicator (magenta, green) and one cell type (fibroblasts) without (cyan). (C) Schematic for biphasic model that captures spheroid formation (black), spheroid growth (green), and from which we form a profile to estimate spheroid formation time (cyan shaded). (D) Early time growth approximated with a linear model. (E-H) Monoculture reduced Greenspan mathematical model. (E,F) Oxygen diffuses within the spheroid and is consumed by living cells which gives rise to gradient in the oxygen partial pressure within the spheroid. Cells are assumed to die below an oxygen partial pressure threshold p_n [%]. (G) Representative confocal microscopy images of the equatorial plane of a M100:F0 spheroid. (H) Simulation of the monoculture reduced Greenspan model. (I-N) Co-culture reduced Greenspan model. (I) Schematic for heterogeneity in the proliferation rates of the two cell types. (J) Schematic for heterogeneity in the loss rates from the necrotic core for the two cell types. (K,L) Oxygen diffuses within the spheroid and is consumed by living cells which gives rise to gradient in the oxygen partial pressure within the spheroid. Melanoma cells and fibroblasts are assumed to die below an oxygen partial pressure thresholds p_{m} [%] and p_{f} [%], respectively. (M) Representative confocal microscopy images of the equatorial plane of a M50:F50 spheroid. (N) Simulation of a co-culture reduced Greenspan model with two oxygen partial pressure thresholds and additional cell migration (green/blue arrows for melanoma/fibroblasts, respectively).

times each cell within the spheroid is able to proliferate and the spheroid grows exponentially. Second, at later times a necrotic core forms, thought to be due to lack of oxygen (Fig 1E,F) [7]. The spheroid then grows to a limiting size and structure where proliferation at the periphery is thought to balance loss from the necrotic core (Fig 1H) [5, 6, 7, 21]. To visualise living and necrotic regions within each spheroid, we use fluorescent ubiquitination-based cell cycle indicator (FUCCI) transduced melanoma cell lines (Fig 1G) [23, 24]. The presence of FUCCI signals indicate living cells and a large central region that lacks FUCCI signals indicates a necrotic core (Fig 1G). We have previously shown that the seminal Greenspan mathematical model describes monoculture spheroid growth remarkably well [5, 6, 7, 21] (Fig 1E-H). Here, we quantitatively directly connect Greenspan's model to co-culture spheroid data for the first time. Alternative mathematical models are reviewed in [25, 26, 27]. For example, individual-based models that prescribe rules that govern the dynamics of each cell [28, 29, 30] or continuum models in the form of partial differential equations [31, 32]. However, these models typically contain parameters that are challenging to estimate using data collected in this study. Further, the biological interpretation of parameters in such models can be unclear.

When we take a purely experimental approach quantitative differences and similarities in co-culture spheroid growth, and the mechanisms giving rise to these similarities and differences, are unclear. For example, how does the addition of a second cell type influence spheroid growth and structure? Further, in our experiments we find that fibroblasts are located throughout the spheroid at early times but are present only in the central region of the spheroid at later times (Fig 1M) [10, 33]. The biological mechanisms driving this process are unclear. For example, it could be that melanoma cells outcompete fibroblasts at the periphery or it could be that melanoma cells migrate to the periphery or fibroblasts actively migrate the centre of the spheroid. To characterise co-culture spheroid growth, we require a framework to capture, test, and explore such observations and hypotheses.

Greenspan's compartment-based mathematical model has played an important role in developing our understanding of monoculture spheroid growth. Each compartment corresponds to a region in the spheroid, for example the periphery or the necrotic core. The model is derived by coupling conservation of volume arguments with geometric constraints that define the boundary of each region. In general, geometric constraints in compartment based spheroid models may be prescribed [17] or derived by considering additional biological mechanisms. In Greenspan's model the geometric constraints arise by considering oxygen diffusion and consumption [21]. Many other compartment-based models have subsequently been developed [17, 25, 26, 27] (Supplementary S5). However, to the best of our knowledge, these models are restricted to one cell type. In this study, we extend a general form of these compartment-based spheroid models subject to general geometric constraints to multiple populations. Then, using this framework, we efficiently and systematically develop multiple two population extensions of Greenspan's model. Exploring these new models reveals biological mechanisms that can describe the co-culture experimental data and those that cannot.

2 Methods

2.1 Experimental methods

We perform two co-culture experiments. The first experiment focuses on spheroid formation and growth. The second experiment focuses on growth characteristics after formation, specifically the temporal evolution of spheroid size, internal structure, and geometry. These experiments are performed for ten days with two human melanoma cell lines (WM983B, 1205Lu) and human primary fibroblasts (QF1696) at five different initial compositions (M100:F0, M75:F25, M50:F50, M25:F75, M0:F100, where Mx:Fy is the initial proportion, measured as a percentage, of melanoma cells x [%] and fibroblasts $y = 100 - x$ [%]). For the first experiment we analyse top-down brightfield images. To quantify spheroid formation and growth we estimate the area enclosed by a projection of the spheroids, A, and assuming a spherical geometry convert these estimates into an equivalent radius ($r = \sqrt{A/\pi}$). For the second experiment we analyse the equatorial plane of each spheroid using confocal microscopy and also capture representative 3D z-stack images of spheroid geometry. The melanoma cell lines were previously transduced with fluorescent ubiquitination-based cell cycle indicator (FUCCI) constructs [23]. Using FUCCI-transduced cell lines allows us to visualise the cell-cycle status of each melanoma cell and identify the necrotic core of each spheroid. Fibroblasts are identified using CellTracker™ Deep Red dye. The fibroblast marker stains the entire cell whereas the FUCCI signal is only present at the cell nucleus. For further details, including cell culture, spheroid generation, imaging procedures and processing, see Supplementary S1-S2.

2.2 Mathematical model to analyse spheroid formation

We analyse spheroid formation using a biphasic model introduced in [14] (Fig 1C). In the first phase, cells that are placed in the well of a tissue culture plate migrate and adhere and the projected area covered by cells shrinks until the spheroid forms (Fig 1A,B). In the second phase, the spheroid grows as a solid mass. We describe each phase using a logistic-type model with distinct parameters,

$$\frac{\mathrm{d}R(t)}{\mathrm{d}t} = \begin{cases} r_1 R(t)\left(1 - \dfrac{R(t)}{\mathcal{R}_1}\right), & 0 \leq t \leq T, \\ r_2 R(t)\left(1 - \dfrac{R(t)}{\mathcal{R}_2}\right), & t > T, \end{cases} \tag{1}$$

where $R(t)$ [μm] describes the equivalent radius of the projected area covered by cells and T [days] is the formation time. In the second phase, $t > T$ [days], $R(t)$ is equivalent to the radius of the spheroid. Further, r_1 [day^{-1}] is associated with the rate at which the spheroid forms; $\mathcal{R}_1$ [μm] is the size of the spheroid at formation; $\mathcal{R}_2$ [μm] is the long-time maximum spheroid radius; r_2 [day^{-1}] is the growth rate of the spheroid as a compact mass; and T [days] is the formation time. The initial spheroid size, $R(0)$ [μm], satisfies $R(0) > \mathcal{R}$ to observe shrinking in the first phase, and $R(t) > \mathcal{R}_1$ for $0 \leq t \leq T$ and $R(t) < \mathcal{R}_2$ for $t > T$. This model is characterised by six parameters $\theta = (R(0), r_1, r_2, \mathcal{R}_1, \mathcal{R}_2, T)$.

2.3 Mathematical model to analyse growth of spheroid size

Focusing on spheroid growth, we do not observe spheroids reaching a long-time maximum size. Therefore, we simplify our analysis and approximate early time exponential growth dynamics in the second phase of the model presented in Eq. (1) with a linear model (Fig 1D, Supplementary S4), i.e. $\exp(\lambda t) = 1 + \lambda t + \mathcal{O}((\lambda t)^2)$ when λt is small [34], to give

$$R(t) = R(T)(1 + \lambda t). \tag{2}$$

where $R(t)$ [μm] is the radius of the spheroid, $R(T)$ [μm] is the radius of the spheroid at the end of formation that we treat as a constant parameter, and λ [day^{-1}] is the growth rate. This model is characterised by two parameters $\theta = (R(T), \lambda)$.

2.4 Mathematical models to analyse growth of spheroid size and structure

In this study we extend a class of one population compartment-based tumour spheroid models to two or more populations (Supplementary S5). These models are derived from conservation of volume arguments that incorporate geometric constraints and biological mechanisms, for example cell proliferation, cell death, and cell migration. Geometric constraints, for example to define the size of proliferating region, may be prescribed [17] or arise by considering additional biological mechanisms, for example oxygen, nutrient, or waste mechanisms [21]. In the following we focus on a reduced version of the seminal Greenspan model [21], introduced by Burton [22]. Different models are are discussed in Supplementary S5.

2.4.1 Monoculture reduced Greenspan model

We consider a reduced version of Greenspan's mathematical model to focus on the temporal evolution of spheroid radius, $R(t)$ [μm], and necrotic core radius, $R_{\mathrm{n}}(t)$ [μm] (Fig 1E-H). We assume that the tumour spheroid is spherically symmetric. The independent variables are radial position, r [μm], and time, t [days]. Growth occurs in two phases. In phase (i) all cells within the spheroid proliferate and the spheroid grows exponentially. In phase (ii) cells at the periphery, $R_{\mathrm{n}}(t) \leq r \leq R(t)$, proliferate while the region $0 \leq r \leq R_{\mathrm{n}}(t)$ is composed of necrotic matter. At later times proliferation at the periphery balances mass loss from the necrotic core resulting in a limiting spheroid structure [5, 6, 21]. To define $R_{\mathrm{n}}(t)$ we consider oxygen mechanisms [7]. Oxygen, reported in terms of oxygen partial pressure $p(r, t)$ [%], diffuses within the spheroid and is consumed by living cells at constant rate per unit volume of cells. We assume that there is an oxygen partial pressure threshold, p_{n} [%], below which cells die. Then $R_{\mathrm{n}}(t)$ is defined implicitly via $p(R_{\mathrm{n}}(t), t) = p_{\mathrm{n}}$, provided the oxygen partial pressure is sufficiently small and $R_{\mathrm{n}}(t) = 0$ otherwise (Fig 1E,F). These oxygen mechanisms give rise to a geometric constraint that defines the size of the proliferating region. Conservation of volume and the geometric constraint gives,

for $t \geq T$ (Supplementary S5.1.2),

$$R^2(t)\frac{\mathrm{d}R(t)}{\mathrm{d}t} = \frac{s}{3}\left[R^3(t) - R_{\mathrm{n}}^3(t)\right] - 3s\gamma R_{\mathrm{n}}^3(t), \tag{3.1}$$

$$\mathcal{R}^2 = R^2(t) - R_{\mathrm{n}}^2(t) - \frac{2R_{\mathrm{n}}^2(t)}{R(t)}\left[R(t) - R_{\mathrm{n}}(t)\right], \tag{3.2}$$

where s [day^{-1}] is the rate at which cell volume is produced by mitosis per unit volume of living cells; γ [-] is a dimensionless parameter associated with loss of mass from the necrotic core; $\mathcal{R}$ [μm] is radius of the spheroid when the necrotic region forms associated with the oxygen partial pressure threshold p_{n} [%]; $R(T)$ [μm] is the initial radius of the spheroid at formation that we treat as a constant parameter; and we set $R_n(T) = 0$ based on experimental observations. This model is characterised by four parameters $\theta = (R(T), s, \gamma, \mathcal{R})$.

2.4.2 Co-culture reduced Greenspan models

We now consider four new co-culture models that are each extensions of the monoculture model: (i) heterogeneity in s; (ii) heterogeneity in γ; (iii) heterogeneity in $\mathcal{R}$; and (iv) heterogeneity in $\mathcal{R}$ and an additional cell migration mechanism. For each model, we assume that the proportion of living cells that undergo necrosis due to lack of oxygen for each cell type is proportional to the volume of cells of that type. Further we introduce $V_{\mathrm{m}}(T)$, the volume of melanoma cells at $t = T$, and treat this as a constant parameter. The volume of fibroblast cells at $t = T$ is then $V_{\mathrm{f}}(T) = 4\pi R(T)^3/3 - V_{\mathrm{m}}(T)$. In the following we outline the new mathematical models. Further details, including the derivation of the governing equations, are presented in Supplementary S5.

Model 1: Heterogeneous s. Here we generalise s [day^{-1}] to be two potentially distinct parameters s_{m} [day^{-1}] and s_{f} [day^{-1}] corresponding to the rates at which cell volume is produced by mitosis per unit volume of living cells for melanoma cells and fibroblasts, respectively (Figure 1I). All other model assumptions and mechanisms are unchanged. This model is characterised by six parameters $\theta = (R(T), V_{\mathrm{m}}(T), s_{\mathrm{m}}, s_{\mathrm{f}}, \gamma, \mathcal{R})$.

Model 2: Heterogeneous γ. Here we generalise γ [-] to be two potentially distinct parameters γ_{m} [day^{-1}] and γ_{f} [day^{-1}]. These parameters are associated with the rate of loss of necrotic matter from the necrotic core from melanoma cells and fibroblasts, respectively (Figure 1J). All other model assumptions and mechanisms are unchanged. This model is characterised by six parameters $\theta = (R(T), V_{\mathrm{m}}(T), s, \gamma_{\mathrm{m}}, \gamma_{\mathrm{f}}, \mathcal{R})$.

Model 3: Heterogeneous $\mathcal{R}$. Here we generalise the single oxygen partial pressure threshold, p_{n} [%], to be two potentially distinct parameters, p_{m} [%] and p_{f} [%], corresponding to the oxygen partial pressure below which melanoma and fibroblast cells die, respectively (Figure 1K,L). We assume $p_{\mathrm{f}} > p_{\mathrm{m}}$ to reproduce experimental observations with regards to the position of fibroblasts within the spheroid during the experiment. These thresholds define two radii $R_{\mathrm{f}}(t) \geq R_{\mathrm{m}}(t)$ implicitly via $p(R_{\mathrm{f}}(t), t) = p_{\mathrm{f}}$ and $p(R_{\mathrm{m}}(t), t) = p_{\mathrm{m}}$, respectively, provided the oxygen partial pressure is sufficiently small, otherwise $R_{\mathrm{f}}(t) = 0$ and/or $R_{\mathrm{m}}(t) = 0$. As we make radial measurements only, we introduce $\mathcal{R}_{\mathrm{m}}$ [μm] and $\mathcal{R}_{\mathrm{f}}$ [μm] which are the size of a monoculture melanoma or monoculture fibroblast spheroid when the oxygen partial

pressure at the centre of the spheroid first reaches p_{m} [%] or p_{f} [%], respectively, i.e. when the necrotic core first forms. These two thresholds give rise to a three phase three compartment model. In phase (i) all cells proliferate and the spheroid grows exponentially. In phase (ii), in $R_{\mathrm{f}}(t) \leq r \leq R(t)$ melanoma cells and fibroblasts proliferate and in $0 \leq r \leq R_{\mathrm{f}}(t)$ melanoma cells proliferate and fibroblasts are necrotic. In phase (iii), in $R_{\mathrm{f}}(t) \leq r \leq R(t)$ melanoma cells and fibroblasts proliferate; in $R_{\mathrm{m}}(t) \leq r \leq R_{\mathrm{f}}(t)$ melanoma cells proliferate while fibroblasts are necrotic; and in $0 \leq r \leq R_{\mathrm{m}}(t)$ all cells are necrotic. This model is characterised by six parameters $\theta = (R(T), V_{\mathrm{m}}(T), s, \gamma, \mathcal{R}_{\mathrm{m}}, \mathcal{R}_{\mathrm{f}})$.

Model 4: Heterogeneous $\mathcal{R}$ and additional cell migration. Here we extend the model with heterogeneous $\mathcal{R}$ to include an additional cell migration mechanism. Fibroblasts are positioned throughout the spheroid at early times but are only present in the central region of the spheroid at later times. To reproduce these observations we assume that living fibroblasts at the periphery of the spheroid, $R_{\mathrm{f}} \leq r \leq R(t)$, migrate towards the centre of the spheroid, $R_{\mathrm{m}} \leq r \leq R_{\mathrm{f}}(t)$, while the same volume of melanoma cells migrate in the opposite direction. There are many biological reasons why this migration could occur and this model does not rule in or out any possibility. To present results, we assume that the rate at which this process occurs is related to the volume of melanoma cells in $R_{\mathrm{m}} \leq r \leq R_{\mathrm{f}}(t)$, the volume of fibroblasts in $R_{\mathrm{f}} \leq r \leq R(t)$, and a new parameter ω. This model is characterised by seven parameters $\theta = (R(T), V_{\mathrm{m}}(T), s, \gamma, \mathcal{R}_{\mathrm{m}}, \mathcal{R}_{\mathrm{f}}, \omega)$.

2.5 Parameter identifiability analysis and estimation

To assess if parameters are practically identifiability and to perform parameter estimation, we use profile likelihood analysis [6, 14, 18, 19]. For this purpose, we consider each model to have two components: (i) a deterministic mathematical model and (ii) a probabilistic observation model, also referred to as an error model, to account for experimental variability and measurement error. Using this approach we assume that experimental measurements are noisy observations of the deterministic mathematical model. We assume that observation errors are independent, identically distributed, additive and normally distributed with zero mean and constant variance σ^2. We estimate σ alongside other model parameters.

For this approach we use the log-likelihood function $\ell(\theta|y^{\mathrm{o}}_{1:J}) = \sum_{j=1}^{J} \log[\phi(y^{\mathrm{o}}_j; y_j(\theta), \sigma^2(\theta))]$, where $\phi(x; \mu, \sigma^2)$ denotes a Gaussian probability density function with mean μ and variance σ^2; θ denotes model parameters; and y^{o}_j denotes the jth experimental observation. For a best-fit to the data we compute the maximum likelihood estimate (MLE), $\hat{\theta} = \sup_{\theta} \ell(\theta|y^{\mathrm{o}}_{1:J})$, subject to bound constraints. Results are reported in terms of the normalised log-likelihood function, $\hat{\ell}(\theta|y^{\mathrm{o}}_{1:J}) = \ell(\theta|y^{\mathrm{o}}_{1:J}) - \sup_{\theta} \ell(\theta|y^{\mathrm{o}})$. Note $\hat{\ell}(\hat{\theta}|y^{\mathrm{o}}_{1:J}) = 0$. To compute profile likelihoods we assume that the full parameter θ can be partitioned into $\theta = (\psi, \lambda)$, where ψ is a scalar interest parameter and λ is a vector nuisance parameter. The profile likelihood for ψ is $\hat{\ell}_p(\psi|y^{\mathrm{o}}) = \sup_{\lambda} \ell(\psi, \lambda|y^{\mathrm{o}}_{1:J})$. Bounds are chosen to ensure that approximate 95% confidence intervals, defined using a profile likelihood threshold value of -1.92 [35], are captured. Mathematical models are solved numerically using the open-source `DifferentialEquations` package in Julia (Supplementary S6). Numerical optimisations are performed using the Nelder–Mead routine in the open-source `NLopt` optimisation package in Julia [36]. For further details see [14].

3 Results and discussion

Here we analyse spheroid formation, geometry, growth, structure in co-culture experiments. Throughout we consider four conditions (M100:F0, M75:F25, M50:F50, M25:F75) that differ with respect to the initial percentages of melanoma and fibroblast cells at the time of seeding. We seek to provide mechanistic insight by analysing experimental measurements within the objective mathematical and statistical modelling framework presented in §2.

3.1 Spheroid formation and geometry

Spheroid experiments are routinely performed to characterise cancer growth. Fibroblasts are commonly included in cancer cell line experiments to enhance spheroid formation and structure. For example, compare the size and densities of 1205Lu monoculture (M100:F0) spheroids and monoculture fibroblast (M0:F100) spheroids (Fig 2A). In both conditions cells initially placed in the well migrate and adhere. The M0:F100 spheroid forms a compact, dense, and approximately spherical structure by approximately 48 hours. In contrast, the M100:F0 spheroid does not (Fig 2B). Experimental images for intermediate conditions, namely M75:F25, M50:F50, and M25:F75, show that fibroblasts enhance formation (Fig 2A,C). We are interested in the contribution of fibroblasts to melanoma spheroids so we do not consider the M0:F100 condition in the remainder of the study.

We now explore the quantitative impact of fibroblasts on melanoma spheroid formation time, T [days], using the biphasic model (§2.2) and profile likelihood analysis (§2.5) to describe the experimental measurements of spheroid size, $R(t)$ (Fig 2D). For each condition, profile likelihoods for T are well-formed and relatively narrow about a single central peak suggesting T is practically identifiable. Three out of the four profiles appear to be consistent suggesting that spheroid formation time relative to the experimental duration is not drastically altered across the conditions (Fig 2E, Table S2). It is not clear if the profile for M25:F75 is different for a biologically meaningful reason or due to experimental noise (Fig 2E). In Supplementary S7.1 we show that, for each condition, experimental data are accurately described by simulating the biphasic mathematical model with the MLE.

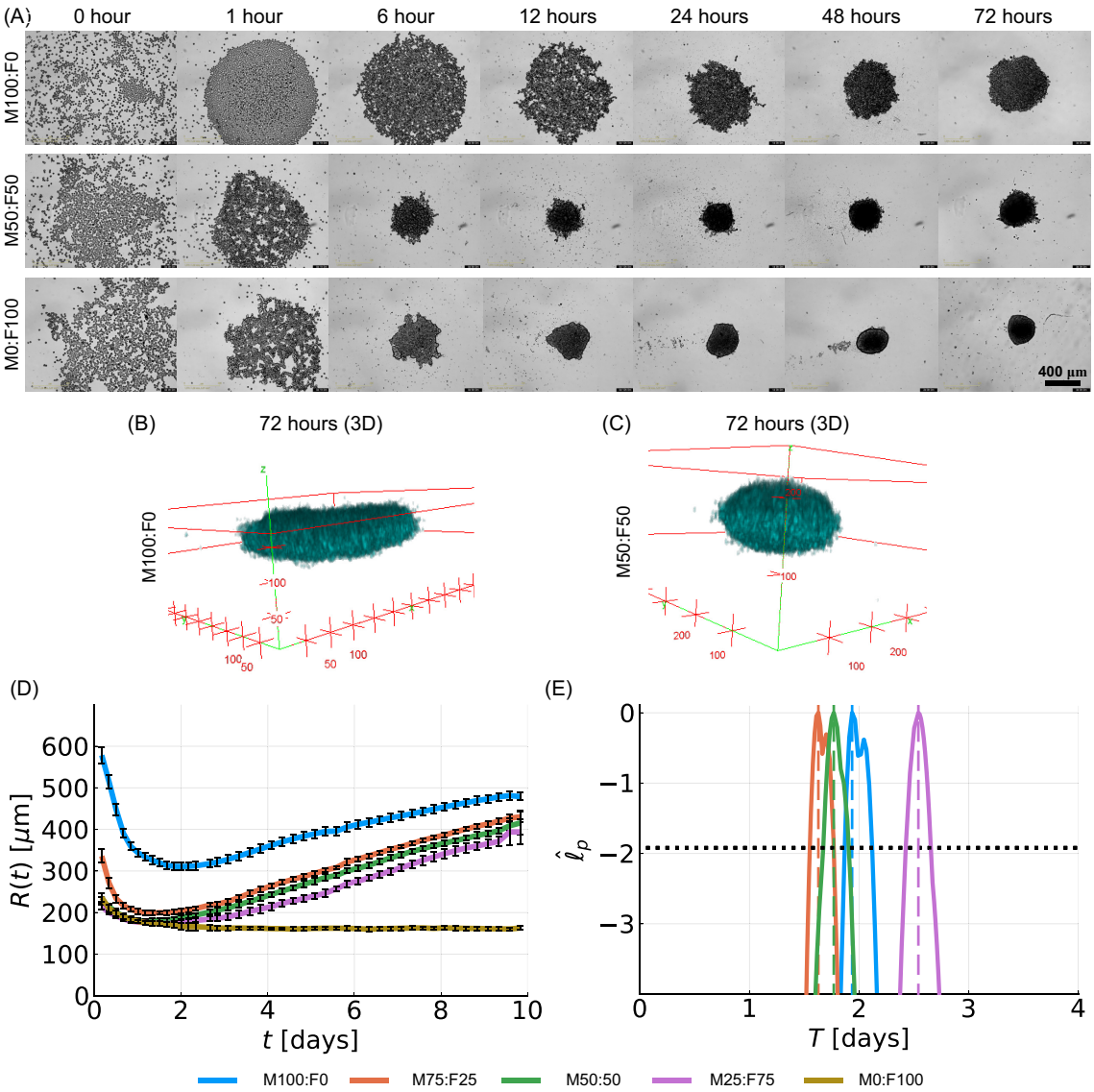

Figure 2: Spheroid formation analysis. Results shown for co-culture spheroids formed with the 1205Lu cell line and fibroblasts. (A) Brightfield top-down experimental images at 0, 1, 6, 24, 48, and 72 [hours]. (B,C) 3D rendering from confocal microscopy z-stack images at 72 hours for (B) M100:F0 and (C) M50:F50 spheroids. The spheroid in (B) is relatively flat while it is reasonable to approximate the spheroid in (C) as spherical. Scale in (B,C) is microns. Colour represents a cell nuclear stain (DAPI) for melanoma cells and fibroblasts. (D) Temporal evolution of measurements of spheroid size, $R(t)$ [μm]. Error bars represent standard deviation about the mean at each time point. (E) Profile likelihoods for formation time, T [days], with approximate 95% confidence interval threshold (horizontal black-dashed). Throughout M100:F0 (blue), M75:F25 (orange), M50:F50 (green), M25:F75 (magenta), and M0:F100 (yellow).

3.2 Temporal evolution of spheroid size

We now focus on co-culture experiments performed using the WM983B melanoma cell line. In contrast to the 1205Lu spheroids, WM983B co-culture spheroids are dense and compact across all conditions (M100:F0, M75:F25, M50:F50, M25:F75) (Fig 3A). The temporal evolution of spheroid size, $R(t)$, is approximately linear in all conditions (Fig 3B). Therefore, we analyse the data using a linear model (Eq (2). Profile likelihoods for $R(3)$ capture that spheroids seeded with a greater proportion of melanoma cells initially form larger spheroids (Fig 3C, Table S3). Profile likelihoods for λ suggest the growth rates are consistent across conditions (Fig 3D, Table S3). Previous monoculture results suggest that increasing the experimental duration results in sigmoidal growth [5, 6, 14].

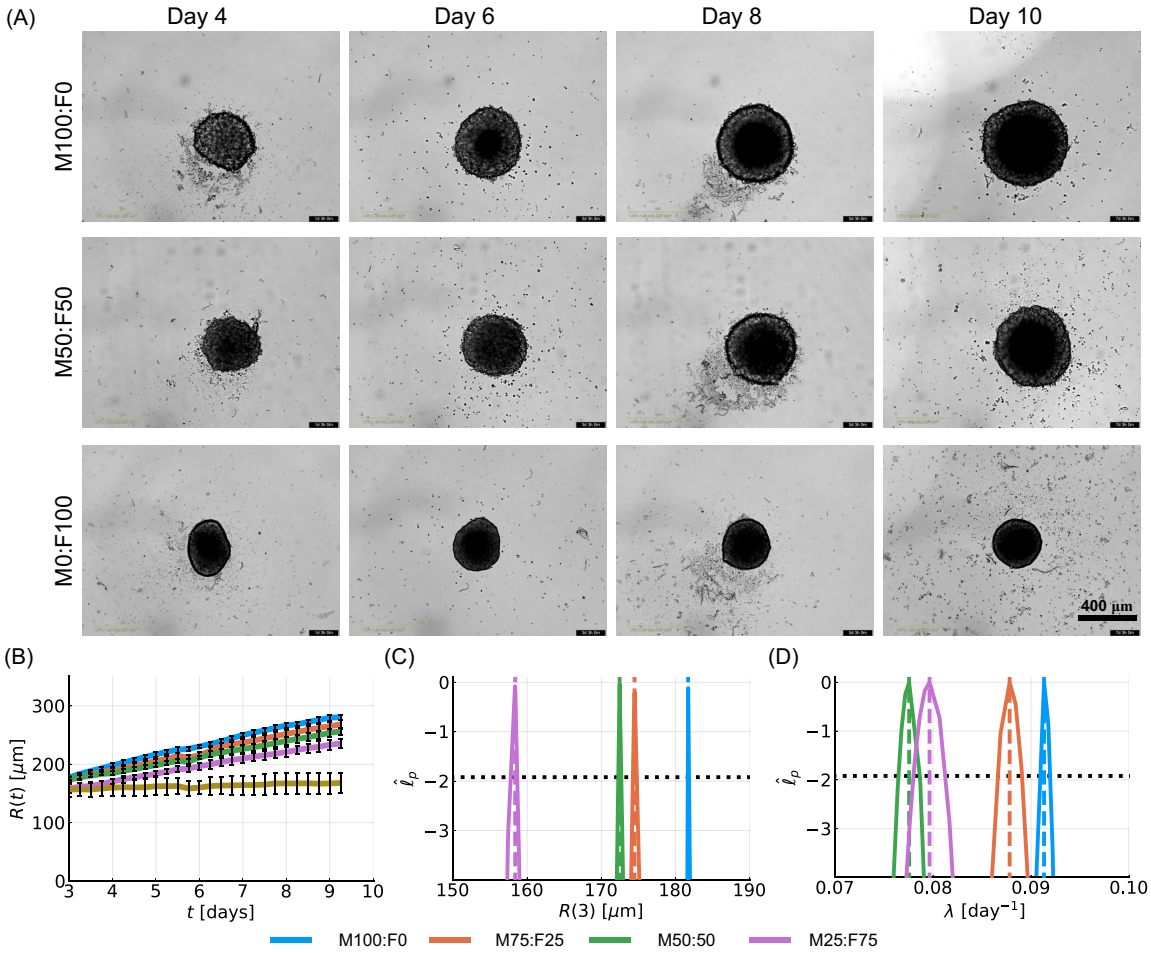

Figure 3: Temporal evolution of spheroid structure. Results shown for co-culture spheroid experiments formed with the WM983B cell line and fibroblasts. (A) Brightfield top-down experimental images. (B) Temporal evolution of overall spheroid size $R(t)$ [µm]. (C) Profile likelihoods for initial spheroid size, $R(3)$ [µm]. (D) Profile likelihoods for growth rate, λ [day^{-1}]. In (C,D) approximate 95% confidence interval threshold shown with horizontal black-dashed line. Throughout conditions are M100:F0 (blue), M75:F25 (orange), M50:F50 (green), M25:F75 (magenta), and M0:F100 (yellow).

3.3 Temporal evolution of spheroid size and structure

Here we explore the role of fibroblasts on melanoma spheroid size and structure. We analyse confocal microscopy images of each spheroid's equatorial plane, measure $R(t)$ and $R_{\mathrm{n}}(t)$, and interpret these data using a series of mathematical models and profile likelihood analysis.

To identify living and proliferating regions within each spheroid we use FUCCI signals. FUCCI signals indicate different stages of the cell cycle: cells in gap 1 (G1) phase fluoresce red, shown in magenta for clarity; and cells in synthesis, gap 2, and mitotic (S/G2/M) phases fluoresce green (Figure 1I). Now consider the FUCCI signals for M100:F0 spheroids (Fig 4A). On days 2 and 3 magenta and green FUCCI signals are present throughout the spheroid indicating all cells are living and proliferating. From day 6 onwards the large central region without FUCCI signals indicates a necrotic core, previously confirmed by both confocal microscopy and flow cytometry using cell death markers [6, 12, 23, 38]. Outside of the necrotic core FUCCI signals indicate a proliferating region at the periphery (predominately green) and an intermediate region of living cells that are proliferation-inhibited (predominately magenta). We observe similar behaviour, albeit the necrotic core forms later, for M75:F25, M50:F50, and M25:F75 spheroids (Fig 4). Using standard image processing techniques we measure $R(t)$ and $R_{\mathrm{n}}(t)$ (Figs 5A-D, Supplementary S2). We focus on $R(t)$ and $R_{\mathrm{n}}(t)$ to present results in terms of typical measurements [6].

Seeking to characterise co-culture spheroid growth, we again turn to mathematical modelling and profile likelihood analysis. We consider a reduced version of Greenspan's mathematical model [21], introduced by Burton [22], and focus on the temporal evolution of $R(t)$ and $R_{\mathrm{n}}(t)$ (§2.4.1). This model is relatively simple. Further, all mechanisms and parameters in the model are biologically interpretable. This is a great advantage over more complicated models where the biological meaning of parameters and mechanisms is not always clear. Note that this mathematical model assumes a monoculture spheroid whereas the experimental data comprise of measurements of co-culture spheroids. We take this approach deliberately. This approach allows us to explore whether estimates of parameters that characterise growth vary across experimental conditions.

For each experimental condition, the monoculture model simulated with the MLE shows excellent agreement with measurements of $R(t)$ and $R_{\mathrm{n}}(t)$ (Figs 5A-D). Profile likelihoods suggest that all model parameters are practically identifiable since the univariate profiles are each well-formed around a single peak (Figs 5E-I). The profile for $R(2)$ [μm] suggests the experimental condition influences the initial size of each spheroid (Fig 5E). Profiles for the proliferation rate per unit volume of living cells, s [day^{-1}], the dimensionless parameter related to the loss rate from the necrotic core, γ [-], and size of the spheroid when the necrotic region forms, $\mathcal{R}$ [μm], appear to be consistent across all conditions (Fig 5F,G,H). Profiles for the standard deviation (Fig 5I) capture variability in the experimental data (Fig 5A-D). These powerful quantitative insights suggest that growth characteristics are similar across conditions. Spheroid structure, assessed by measuring the necrotic fraction, $R_{\mathrm{n}}(t)/R(t)$ [-], also appears to be consistent across conditions (Fig 5J).

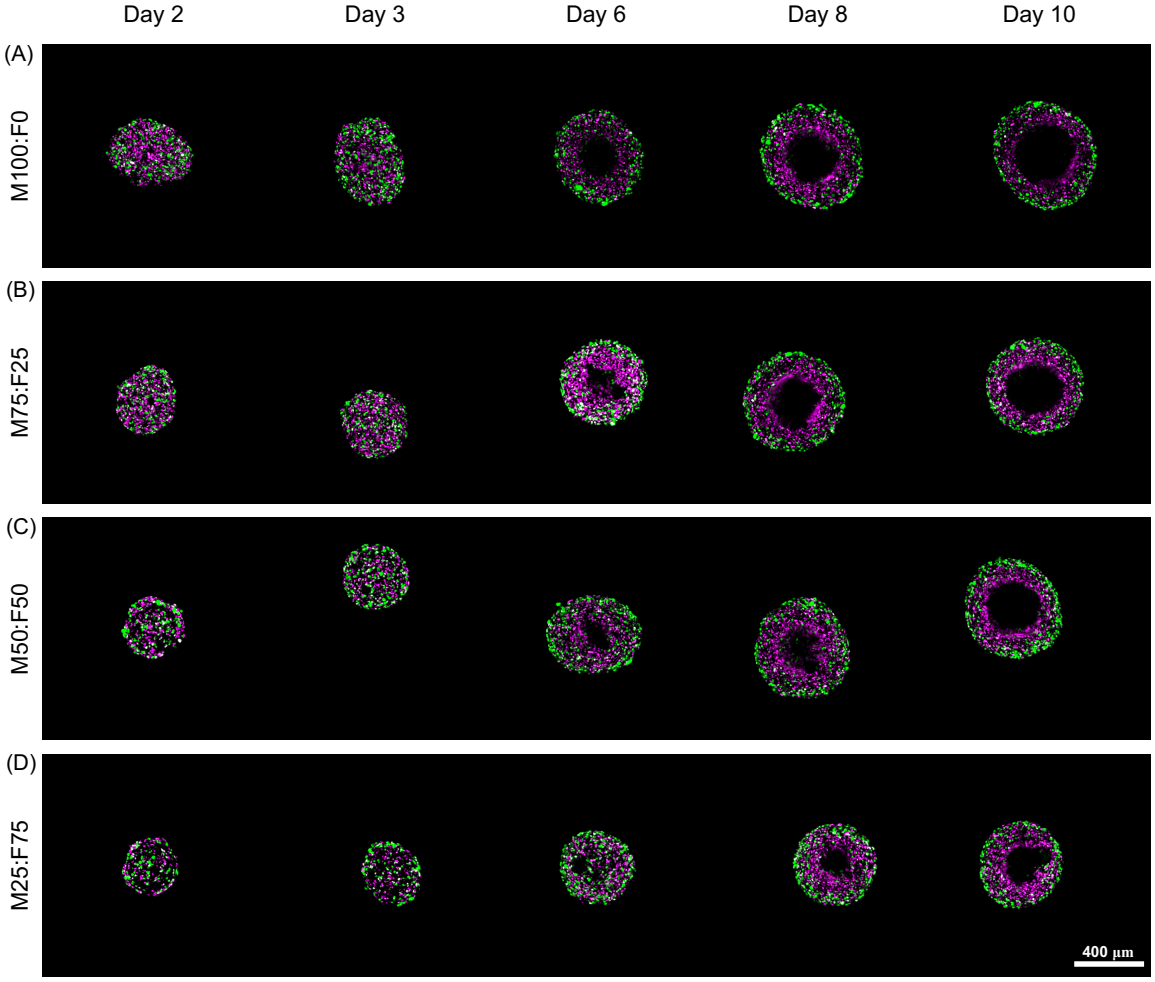

Figure 4: Spatio-temporal evolution of tumour spheroid structure. Confocal microscopy images of each spheroid's equatorial plane for (A) M100:F0, (B) M75:F25, (C) M50:F50, and (D) M25:F75 spheroids. Results shown for the WM983B melanoma cell line. FUCCI signals are shown with magenta and green. Presence of FUCCI signal indicates living cells whereas large regions at the centre of spheroids that lack FUCCI signals indicate a necrotic core. Fibroblasts are not shown so that it is easier to visualise the necrotic core and overall size.

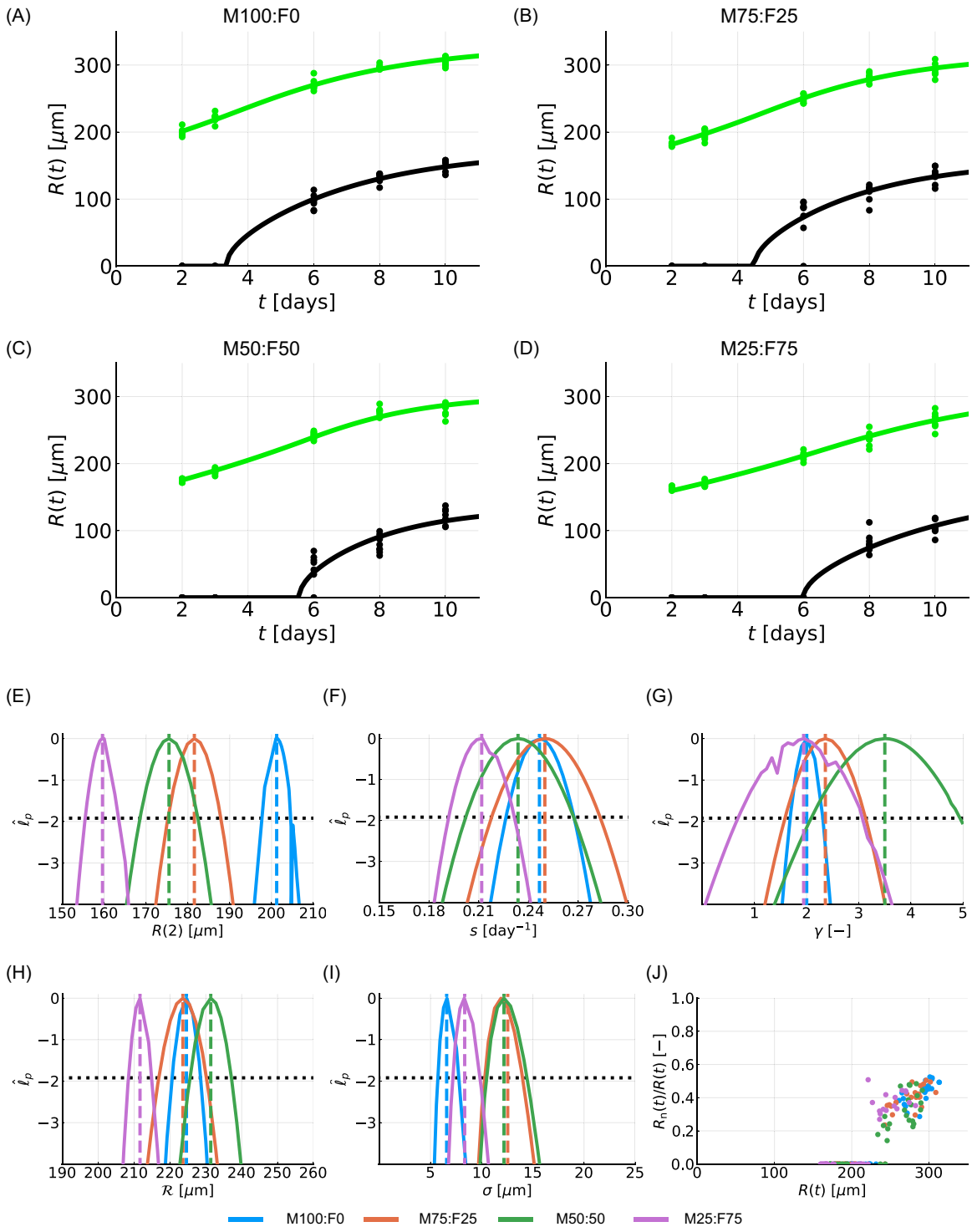

Figure 5: Temporal evolution of spheroid size and structure analysed using the reduced Greenspan mathematical model. (A-D) Comparison of experimental data and mathematical model simulated with the maximum likelihood estimate for: (A) M100:F0; (B) M75:F25; (V) M50:F50; (D) M25:F75 spheroids. In (A-D) experimental measurements of spheroid radius, $R(t)$ [μm], and necrotic radius, $R_{\mathrm{n}}(t)$ [μm], shown as green and black circles, respectively. (E-H) Profile likelihoods for (E) $R(T)$ [μm]; (F) s [day^{-1}]; (G) γ [-]; (H) $\mathcal{R}$ [μm], and (I) σ [μm]. In (E-I) approximate 95% confidence interval threshold shown with horizontal black-dashed line. (J) Measurements of the necrotic fraction, $R_{\mathrm{n}}(t)/R(t)$ [-], against spheroid radius, $R(t)$ [μm]. Throughout conditions are M100:F0 (blue), M75:F25 (orange), M50:F50 (green), and M25:F75 (magenta).

Thus far we have examined the experimental images using FUCCI signals to identify regions of living melanoma cells, that are proliferating or proliferation-inhibited, and necrotic matter. Here, we re-examine these experimental images and include the signal from the fibroblast marker (Fig 6, Supplementary S3.2). Focusing on the M75:F25, M50:F50, and M25:F75 spheroids, fibroblasts are present throughout each spheroid on days 2 and 3 (Fig 6B,C,D). At later times we only observe fibroblasts close to the centre of the spheroid. The biological mechanisms driving the changing position of the fibroblasts within the spheroid are unclear. Seeking further insights we again turn to mathematical modelling and systematically extend the monoculture reduced Greenspan model.

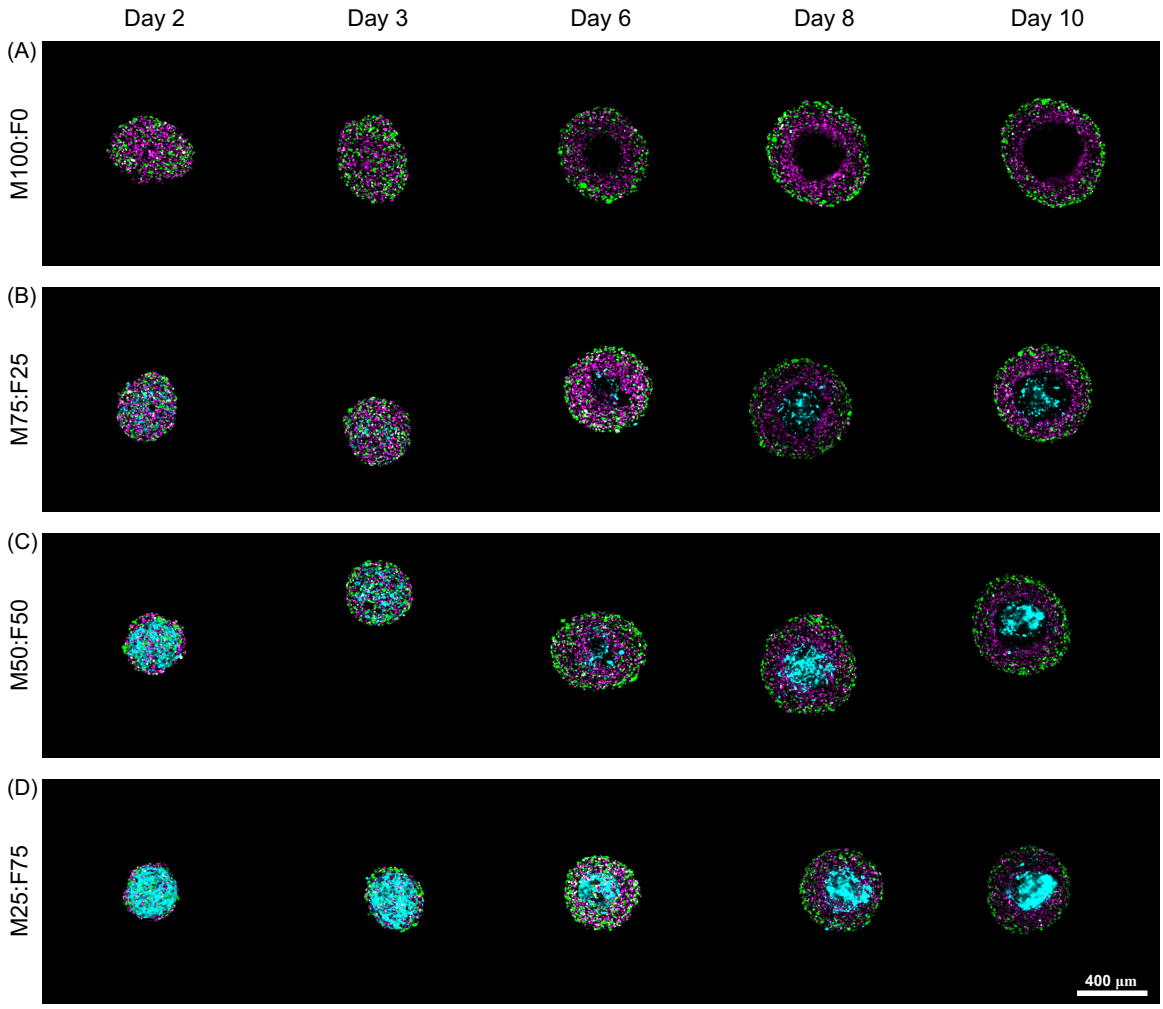

Figure 6: Spatio-temporal evolution of tumour spheroid structure including fibroblast marker. Confocal microscopy images of each spheroid's equatorial plane for (A) M100:F0, (B) M75:F25, (C) M50:F50, and (D) M25:F75 spheroids. These are same spheroids as shown in Fig (4) now with the fibroblast marker shown in cyan. The fibroblast marker stains the entire cell whereas the FUCCI signal is only present at the cell nucleus.

We systematically extend the monoculture model by introducing heterogeneity into s, γ, and $\mathcal{R}$ independently and in turn. This results in four new models: (i) heterogeneity in s; (ii) heterogeneity in γ; (iii) heterogeneity in $\mathcal{R}$; and (iv) heterogeneity in $\mathcal{R}$ and an additional cell migration mechanism. To derive and solve each of these new models we use our new general compartment-based spheroid modelling framework (§2.4.2, Supplementary S5). In the following, parameter values are chosen to capture, where possible, loss of fibroblasts from the periphery and chosen so that model simulations agree with measurements of $R(t)$ and $R_n(t)$ from the M50:F50 condition. Similar results are obtained for M75:F25 and M25:F75 conditions.

In Model 1 we assume that melanoma cells and fibroblasts proliferate at different rates per unit volume, s_{m} [day^{-1}] and s_{f} [day^{-1}], respectively (§2.4.2, Fig 1I). Simulating Model 1 with $s_{\mathrm{m}} > s_{\mathrm{f}}$ we can capture the temporal evolution of $R(t)$ and $R_{\mathrm{n}}(t)$ (Fig 7A). For greater insight, we analyse the temporal evolution of the volume of melanoma cells and fibroblasts within each region $j = 1, 2$ of the spheroid, denoted $V_{\mathrm{m}}^{(j)}(t)$ and $V_{\mathrm{f}}^{(j)}(t)$, respectively. Here region one is the periphery, $R_{\mathrm{n}}(t) < r < R(t)$, and region two is the necrotic core, $0 < r < R_{\mathrm{n}}(t)$. For each region the melanoma fraction is $\phi_{\mathrm{m}}^{(j)}(t) = V_{\mathrm{m}}^{(j)}(t)/[V_{\mathrm{m}}^{(j)}(t) + V_{\mathrm{f}}^{(j)}(t)]$. Since $\phi_{\mathrm{m}}^{(1)}(t) \to 1$ as $t \to \infty$, Model 1 captures the loss of fibroblasts from the periphery (Fig 7B). Further, since $\phi_{\mathrm{m}}^{(2)}(t) \to 1$ as $t \to \infty$, Model 1 suggests that the necrotic core will eventually be composed only of matter from necrotic melanoma cells (Fig 7B). This is a useful insight. In experimental images we are unable to quantify the proportion of necrotic matter from melanoma cells and fibroblasts due to loss of signal during necrosis.

In Model 2, we assume the rate at which mass in the necrotic core degrades and is lost from the spheroid depends on whether the necrotic matter is from melanoma cells or fibroblasts (Fig 1J). This is associated with two parameters γ_{m} [-] and γ_{f} [-]. Simulating Model 2 we can capture the temporal evolution of $R(t)$ and $R_{\mathrm{n}}(t)$ but we cannot capture the loss of fibroblasts at the periphery (Fig 7C,D).

In Models 3 and 4, we generalise the single oxygen partial pressure threshold, p_{n} [%], with two thresholds, $p_{\mathrm{f}} \geq p_{\mathrm{m}}$ [%], corresponding to the oxygen partial pressure below which fibroblasts and melanoma cells die, respectively (Fig 1K,L). These two thresholds define $R_{\mathrm{f}}(t) \geq R_{\mathrm{m}}(t)$, respectively (Fig 1N), and two parameters ($\mathcal{R}_{\mathrm{f}}$, $\mathcal{R}_{\mathrm{m}}$). This gives rise to a model with three compartments (Fig 1I-N). Here we assume that measurements of the necrotic core correspond to measurements of $R_{\mathrm{m}}(t)$ that is defined by p_{m}. This is because we measure the size of the necrotic region using FUCCI signals from melanoma cells. Similarly to Model 2, with Model 3 we can capture the temporal evolution of $R(t)$ and $R_{\mathrm{m}}(t)$ (Fig 7E) but cannot capture the loss of fibroblasts at the periphery (Fig 7F).

Introducing additional cell migration into Model 3 gives Model 4. We assume that living fibroblasts at the periphery, $R_{\mathrm{f}}(t) \leq r \leq R(t)$, migrate towards the centre of the spheroid, $R_{\mathrm{m}}(t) \leq r \leq R_{\mathrm{f}}(t)$, while the same volume of melanoma cells migrate in the opposite direction (Fig 1N). This can give rise to transient dynamics where the number of fibroblasts at the core increases and long-term loss of fibroblasts from the periphery (Fig 7G,H). There are many biological reasons why this migration could occur and this model does not rule in or out any possibility. Results for co-culture spheroids with the 1205Lu cell line suggest that fibroblasts can form the core of spheroids at earlier times (Supplementary S7.3).

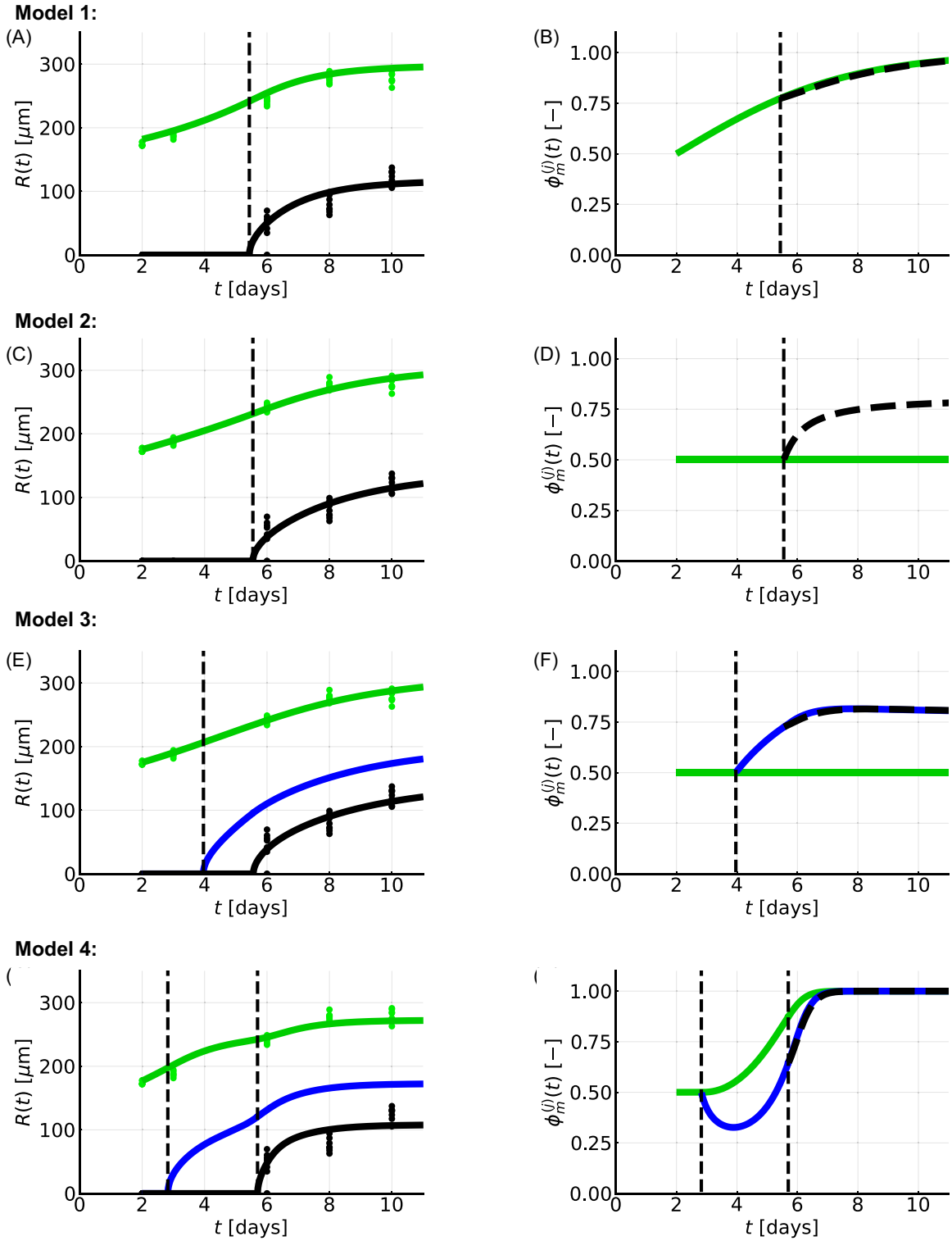

Figure 7: Spatio-temporal evolution of spheroid structure analysed using multiple co-culture reduced Greenspan models. (A,C,E,G) Simulations of (A) Model 1, (C) Model 2, (E) Model 3, (G) Model 4 show the temporal evolution of spheroid size $R(t)$ (green). For Models 1 and 2 we present the size of necrotic core $R_{\mathrm{n}}(t)$ (black). For Models 3 and 4 we present $R_{\mathrm{f}}(t)$ (blue) and $R_{\mathrm{m}}(t)$ (black). Experimental measurements of $R(t)$ and necrotic core from M50:F50 spheroids are shown as green and black circles, respectively. (B,D,F,H) Temporal evolution of melanoma fraction $\phi_{\mathrm{m}}^{(j)}(t) = V_{\mathrm{m}}^{(j)}(t)/[V_{\mathrm{m}}^{(j)}(t) + V_{\mathrm{f}}^{(j)}(t)]$ for regions $j = 1$ (green), 2 (black dashed) in Models 1 and 2, and $j = 1$ (green), 2 (black dashed), 3 (blue) in Models 3 and 4.

4 Conclusions

In this study we develop a general mathematical and statistical framework to characterise and interpret co-culture spheroid formation and growth. The work includes novel theoretical and biological contributions. We perform a series of co-culture spheroid experiments and use our mathematical and statistical modelling framework to quantify spheroid formation time and estimate key parameters that characterise growth. We find that in our experiments introducing a second cell type allows a cancer cell line to generate spheroids with approximately spherical structures that would not otherwise. Further, we find that the second cell type has limited impact on formation time, spheroid growth and structure. There are many possible reasons for these results. For example it could be that there are limited interactions, or cross-talk, between the melanoma cells and fibroblasts. As part of this analysis we quantitatively directly connect the seminal Greenspan model to co-culture spheroid data for the first time. We choose to use a monoculture model to describe co-culture data deliberately. This approach allows us to explore whether estimates of parameters that characterise growth vary across experimental conditions and we find this to be insightful. In addition, by extending a general class of monoculture compartment-based mathematical models to multiple populations, we reveal biological mechanisms that can describe the internal dynamics of co-culture spheroids and those that cannot. This framework is important because there is, at present, no widely used and commonly accepted framework for modelling and interpreting co-culture spheroid growth where nutrient limitations and geometric constraints play a role in constraining spheroid growth.

Our mathematical and statistical modelling framework can be applied to different cell types and to spheroids grown in different conditions. Here we choose to perform experiments with melanoma cells and fibroblasts. This builds on our previous monoculture melanoma spheroid studies [5, 6, 14, 23]. Our results are consistent with analysis of two-dimensional experiments which suggest that fibroblasts have a limited impact on co-culture melanoma spreading and invasion [37]. However, we note that other spheroid studies suggest fibroblasts contribute to melanoma spheroid growth [11]. Interesting future work would be to explore these differences. Such differences could arise due to many reasons, for example choice of cell line, fibroblasts, and experimental conditions. Further, the framework is well-suited to diagnose cross-talk in other co-culture experiments.

In our WM983B co-culture experiments fibroblasts are present throughout the spheroid at early times but are only present in the central region of the spheroid at later times [10, 33]. Using our new mathematical models we identify that differences in proliferation rates, or differences in when each cell undergoes necrosis due to lack of oxygen in combination with cell migration, could drive this behaviour. Performing additional experiments to inhibit proliferation or growing co-culture spheroids in different oxygen conditions may be insightful [14]. In general, additional data would be helpful to assess whether parameter identifiability in the co-culture mathematical models. Our framework is well-suited to incorporate such additional data and, if appropriate, different error models [18].

The co-culture mathematical modelling framework presented in Supplementary S5 is general. We use this framework primarily to extend the monoculture reduced Greenspan mathematical model to two

populations. This allows us to explore the temporal evolution of co-culture spheroid size and structure. In Supplementary S5 we extend a different monoculture model to two populations, the radial-death model [17]. The radial-death model captures key features of Greenspan's model, but rather than considering oxygen mechanisms prescribes a fixed size for the proliferating region. Many other models could be considered with additional compartments and/or mechanisms such as nutrient/waste diffusion and consumption/production. For example, we could use our experimental images to identify regions where melanoma cells are proliferation-inhibited and incorporate this into mathematical modelling [5, 6, 14, 21]. In general, the additional complexity of these models may result in parameter identifiability challenges with currently available data [17, 19]. Incorporating mechanical effects is also of interest [39, 40]. The framework could also be extended to characterise the effectiveness of chemotherapies and radiotherapies [8, 9, 10, 11]. Overall, this study lays a theoretical foundation to characterise co-culture tumour spheroid formation and growth.

Data availability

The datasets generated and analysed during this study are summarised in the electronic supplementary material and are available on a GitHub repository (https://github.com/ryanmurphy42/Murphy2022CoCulture).

Code Availability

Key computer code and all experimental data used to generate computational results are available on a GitHub repository (https://github.com/ryanmurphy42/Murphy2022CoCulture).

Author's contributions

All authors conceived and designed the study. RJM performed the research and drafted the article. GG performed experimental work. All authors provided comments and approved the final version of the manuscript. NKH and MJS contributed equally.

Competing interests

We declare we have no competing interest.

Funding

MJS and NKH are supported by the Australian Research Council (DP200100177). The funders had no role in study design, data collection and analysis, decision to publish, or preparation of the manuscript.

Acknowledgements

We thank Associate Professor Rick Sturm, Frazer Institute (University of Queensland) for providing the fibroblasts. We thank John Blake for guidance using IncuCyte. This research was carried out at the Translational Research Institute (TRI), Woolloongabba, QLD. TRI is supported by a grant from the Australian Government. We thank the staff in the microscopy core facility at TRI for their technical support. We thank Professor Atsushi Miyawaki, RIKEN, Wako-city, Japan, for providing the FUCCI constructs, and Professor Meenhard Herlyn, The Wistar Institute, Philadelphia, PA, for providing the cell lines.

References

[1] Costa EC, Moreira AF, de Melo-Diogo D, Gaspar VM, Carvalho MP, Correia IJ. 2016. 3D tumor spheroids: An overview on the tools and techniques used for their analysis. Biotechnology Advances. 34, 1427-1441. (doi:10.1016/j.biotechadv.2016.11.002)

[2] Hirschhaeuser F, Menne H, Dittfled C, West J, Mueller-Klieser W, Kunz-Schughart LA. 2010. Multicellular tumor spheroids: An underestimated tool is catching up again. Journal of Biotechnology. 148, 3-15. (doi:10.1016/j.jbiotec.2010.01.012)

[3] Mehta G, Hsiao AY, Ingram M, Luker GD, Takayama S. 2012. Opportunities and challenges for use of tumor spheroids as models to test drug delivery and efficacy. Journal of Controlled Release. 10, 192-204. (doi:10.1016/j.jconrel.2012.04.045)

[4] Beaumont KA, Mohana-Kumaran N, Haass NK. 2014. Modeling Melanoma In Vitro and In Vivo. Healthcare. 2, 27-46. (doi:10.3390/healthcare2010027)

[5] Browning AP, Sharp JA, Murphy RJ, Gunasingh G, Lawson B, Burrage K, Haass NK, Simpson MJ. 2021. Quantitative analysis of tumour spheroid structure. eLife. 10, e73020. (doi:10.7554/eLife.73020)

[6] Murphy RJ, Browning AP, Gunasingh G, Haass NK, Simpson MJ. 2022. Designing and interpreting 4D tumour spheroid experiments. Communications Biology. 5, 91. (doi:10.1038/s42003-022-03018-3)

[7] Murphy RJ, Gunasingh G, Haass NK, Simpson MJ. 2022. Growth and adaptation mechanisms of tumour spheroids with time-dependent oxygen availability. To appear PLoS Computational Biology. (doi:10.1101/2022.04.24.489294)

[8] Tofilon PJ, Buckley N, Deen DF. 1984. Effect of cell-cell interactions on drug sensitivity and growth of drug-sensitive and-resistant tumor cells in spheroids. Science. 226, 862-864. (doi:10.1126/science.6494917)

[9] Paczkowski M, Kretzschmar WW, Markelc B, Liu SK, Kunz-Schughart LA, Harris AL, Partridge M, Byrne HM, Kannan P. 2021. Reciprocal interactions between tumour cell populations enhance growth and reduce radiation sensitivity in prostate cancer. Communications Biology. 4, 6. (doi:10.1038/s42003-020-01529-5)

[10] Yakavets I, Francois A, Benoit A, Merlin J-L, Bezdetnaya L, Vogin G. 2020. Advanced co-culture 3D breast cancer model for investigation of fibrosis induced by external stimuli: optimization study. Scientific Reports. 10, 21273. (doi:10.1038/s41598-020-78087-7)

[11] Flach EH, Rebecca VW, Herlyn M, Smalley KS, Anderson AR. 2011. Fibroblasts contribute to melanoma tumor growth and drug resistance. Molecular Pharmaceutics. 8, 2039-2049. (doi:10.1021/mp200421k)

[12] Spoerri L, Gunasingh G, Haass NK. 2021. Fluorescence-based quantitative and spatial analysis of tumour spheroids: a proposed tool to predict patient-specific therapy response. Frontiers in Digital Health. 3, 668390. (doi:10.3389/fdgth.2021.668390)

[13] Spoerri L, Beaumont KA, Anfosso A, Haass NK. 2017. Real-time cell cycle imaging in a 3D cell culture model of melanoma. Methods in Molecular Biology. 1612, 401–416. (doi:10.1007/978-1-4939-7021-6_29)

[14] Murphy RJ, Maclaren OJ, Calabrese AR, Thomas PB, Warne DJ, Williams ED, Simpson MJ. 2022. Computationally efficient framework for diagnosing, understanding, and predicting biphasic population growth Journal of the Royal Society Interface. 19, 20220560 (doi:10.1098/rsif.2022.0560)

[15] Gerlee P. 2013. The model muddle: In search of tumor growth laws. Cancer Research. 73, 2407-2411. (doi:10.1158/0008-5472.CAN-12-4355)

[16] Sarapata EA, de Pillis LG. 2014. A comparison and catalog of intrinsic tumor growth models. Bulletin of Mathematical Biology. 76, 2010-2024. (doi:10.1007/s11538-014-9986-y)

[17] Browning AP, Simpson MJ. 2022. Geometric analysis enables biological insight from complex non-identifiable models using simple surrogates. To appear PLoS Computational Biology. (doi:10.48550/arXiv.2208.01868)

[18] Pawitan Y. 2001. In All Likelihood: Statistical Modelling And Inference Using Likelihood. Oxford, UK: Oxford University Press.

[19] Simpson MJ, Baker RE, Vittadello ST, Maclaren OJ. 2020. Practical parameter identifiability for spatio-temporal models of cell invasion. Journal of the Royal Society Interface. 17, 2020055. (doi:10.1098/rsif.2020.0055)

[20] Raue A, Kreutz C, Maiwald T, Bachmann J, Schilling M, Klingmüller U, Timmer J. 2009. Structural and practical identifiability analysis of partially observed dynamical models by exploiting the profile likelihood. Bioinformatics. 25, 1923-1929. (doi:10.1093/bioinformatics/btp358).

[21] Greenspan HP. 1972. Models for the growth of a solid tumor by diffusion. Studies in Applied Mathematics. 51, 317-340. (doi:10.1002/sapm1972514317)

[22] Burton AC. 1966. Rate of growth of solid tumours as problem of diffusion. Growth. 30, 157-176.

[23] Haass NK, Beaumont KA, Hill DS, Anfosso A, Mrass P, Munoz MA, Kinjyo I, Weninger W. 2014. Real-time cell cycle imaging during melanoma growth, invasion, and drug response. Pigment Cell & Melanoma Research. 27, 764-76. (doi:10.1111/pcmr.12274)

[24] Sakaue-Sawano A, Kurokawa H, Morimura T, Hanyu A, Hama H, Osawa H, Kashiwagi S, Fukami K, Miyata T, Miyoshi H, et al. 2008. Visualizing spatiotemporal dynamics of multicellular cell-cycle progression. Cell. 132, 487-98. (doi:10.1016/j.cell.2007.12.033)

[25] Araujo RP, McElwain DLS. 2004. A history of the study of solid tumour growth: the contribution of mathematical modelling. Bulletin of Mathematical Biology. 66, 1039-1091. (doi:10.1016/j.bulm.2003.11.002)

[26] Bull JA, Byrne HM. 2022. The hallmarks of mathematical oncology. Proceedings of the IEEE. 110, 523-540. (doi:10.1109/JPROC.2021.3136715)

[27] Lowengrub JS, Friebos HB, Jin F, Chuang Y-L, Li X, Macklin P, Wise SM, Cristini V. 2010. Nonlinear modelling of cancer bridging the gap between cells and tumours. Nonlinearity. 23, 1-91. (doi:10.1088/0951-7715/23/1/R01)

[28] Bull JA, Mech F, Quasier T, Waters SL, Byrne HM. 2020. Mathematical modelling reveals cellular dynamics within tumour spheroids. PLoS Computational Biology. 16, e1007961. (doi:10.1371/journal.pcbi.1007961)

[29] Klowss JJ, Browning AP, Murphy RJ, Carr EJ, Plank MJ, Gunasingh G, Haass NK, Simpson MJ. 2022. A stochastic mathematical model of 4D tumour spheroids with real-time fluorescent cell cycle labelling. Journal of the Royal Society Interface. 19, 20210903. doi:10.1098/rsif.2021.0903

[30] Jagiella N, Müller B, Müller M, Vignon-Clementel IE, Drasdo D. 2016. Inferring growth control mechanisms in growing multi-cellular spheroids of NSCLC cells from spatial-temporal image data. PLoS Computational Biology. 12, e1004412. (doi:10.1371/journal.pcbi.1004412)

[31] Ward JP, King JR. 1997. Mathematical modelling of avascular-tumour growth II: modelling growth saturation. Mathematical Medicine and Biology: A Journal of the IMA. 16, 171-211. (doi:10.1093/imammb/16.2.171)

[32] Jin W, Spoerri L, Haass NK, Simpson MJ. 2021. Mathematical model of tumour spheroid experiments with real-time cell cycle imaging. Bulletin of Mathematical Biology. 83, 1-23. (doi:10.1007/s11538-021-00878-4)

[33] Fang G, Lu H, Law A, Gallego-Ortega D, Jin D, Lin G. 2019. Gradient-sized control of tumor spheroids on a single chip. Lab Chip. 19, 4093-4103. (doi:10.1039/C9LC00872A)

[34] Browning AP, McCue SW, Simpson MJ. 2017. A Bayesian computational approach to explore the optimal duration of a cell proliferation assay. Bulletin of Mathematical Biology. 79, 1888-1906 (doi: 10.1007/s11538-017-0311-4)

[35] Royston P. 2007. Profile likelihood for estimation and confidence intervals. Stata J. 7, 376–387. (doi:10.1177/1536867X0700700305)

[36] Johnson SG. 2022. The NLopt module for Julia. Retrieved 11-Dec-2022 NLopt.

[37] Haridas P, Penington CJ, McGovern JA, McElwain DLS, Simpson MJ. 2017. Quantifying rates of cell migration and cell proliferation in co-culture barrier assays reveals how skin and melanoma cells interact during melanoma spreading and invasion. Journal of Theoretical Biology. 423, 13-25. (doi:10.1016/j.jtbi.2017.04.017)

[38] Spoerri L, Tonnessen-Murray CA, Gunasingh G, Hill DS, Beaumont KA, Jurek RJ, Chauhan J, Vanwalleghem GC, Fane ME, Daignault-Mill SM, et al. 2021. Phenotypic melanoma heterogeneity is regulated through cell-matrix interaction dependent changes in tumor microarchitecture. Preprint on bioRxiv. (doi:10.1101/2020.06.09.141747)

[39] Loessner D, Flegg JA, Byrne HM, Clements JA, Hutmacher DW. 2013. Growth of confined cancer spheroids: a combined experimental and mathematical modelling approach. Integrative Biology. 5, 597-605. (doi:10.1039/c3ib20252f)

[40] Walker BJ, Celora GL, Goriely A, Moulton DE, Byrne HM. 2022. Towards a minimal admissible model of solid tumour spheroid growth. Preprint on arXiv. (doi:10.48550/arXiv.2206.13818)